

A&A manuscript no.
(will be inserted by hand later)

Your thesaurus codes are:
08.23.2; 08.09.2; 08.02.2; 08.13.2; 08.22.3; 08.03.4

ASTRONOMY
AND
ASTROPHYSICS

Abundance correlations in mildly metal-poor stars^{*}

E. Jehin, P. Magain^{**}, C. Neuforge^{***}, A. Noels, G. Parmentier and A. A. Thoul

Institut d'Astrophysique et de Géophysique, Université de Liège, 5, Avenue de Cointe, B-4000 Liège, Belgium

Received date; accepted date

Abstract. Accurate relative abundances have been obtained for a sample of 21 mildly metal-poor stars from the analysis of high resolution and high signal-to-noise spectra. In order to reach the highest coherence and internal precision, lines with similar dependency on the stellar atmospheric parameters were selected, and the analysis was carried out in a strictly differential way within the sample.

With these accurate results, correlations between relative abundances have been searched for, with a special emphasis on the neutron capture elements.

This analysis shows that the r elements are closely correlated to the α elements, which is in agreement with the generally accepted idea that the r -process takes place during the explosion of massive stars.

The situation is more complex as far as the s elements are concerned. Their relation with the α elements is not linear. In a first group of stars, the relative abundance of the s elements increases only slightly with the α elements overabundance until the latter reaches a maximum value. For the second group, the s elements show a rather large range of enhancement and a constant (and maximum) value of the α elements overabundance.

This peculiar behaviour leads us to distinguish between two sub-populations of metal-poor stars, namely Pop IIa (first group) and Pop IIb (second group).

We suggest a scenario of formation of metal-poor stars based on two distinct phases of chemical enrichment, a first phase essentially consisting in supernova explosions of massive stars, and a second phase where the enrichment is provided by stellar winds from intermediate mass stars. More specifically, we assume that all thick disk and field halo stars were born in globular clusters, from which they escaped, either during an early disruption of the cluster (Pop IIa) or, later, through an evaporation process (Pop IIb).

Send offprint requests to: E. Jehin

^{*} Based on observations obtained at the European Southern Observatory, La Silla, Chile.

^{**} Maître de Recherches au Fonds National de la Recherche Scientifique (Belgium)

^{***} Chargé de Recherches au Fonds National de la Recherche Scientifique (Belgium)

Key words: Stellar abundances – Population II stars – Nucleosynthesis – Neutron capture elements – Chemical evolution of the Galaxy

1. Introduction

The chemical composition of the solar system is now known with a high accuracy from the spectroscopic studies of the solar photosphere as well as from the analysis of the carbonaceous chondrites (Anders and Grevesse 1989, Grevesse et al. 1996). Moreover, theoretical models of stellar evolution and nucleosynthesis allow the identification of the most likely sites and mechanisms for the formation of the chemical elements. Combining them with simple models for the chemical evolution of the Galaxy, one can reproduce reasonably well the solar system abundances.

However, the solar system only provides a single data point, both in the time evolution of the Galaxy and in the spatial distribution in the disk. It is thus important to gather additional data in order to have an insight of the chemical composition of the interstellar matter at different epochs since the formation of the Galaxy.

As time goes by, more and more metals are synthesized in the stellar interiors and ejected in the surrounding environment, so that the overall metallicity slowly increases. Although the correlation of metallicity with time is not a perfect one, unevolved metal-poor stars give a picture of the chemical conditions at earlier phases of the galactic evolution.

Up to now, spectroscopic analyses of metal-poor stars have essentially consisted in determining abundance ratios as a function of metallicity. These ratios are supposed to show the evolution of the nucleosynthetic processes with time. Unfortunately, these results generally show a rather large scatter, which is either of cosmic origin or due to observational uncertainties. In the latter case, this prevents any meaningful comparison with the theoretical models. On the other hand, if the scatter reflects an intrinsic cosmic dispersion, it should be accounted for in the models.

Table 1. Basic photometric data

HD	ID	V	b−y	V−K	c_1
22879	1	6.70	0.366	1.478	0.274
25704	2	8.12	0.371	1.53	0.275
59984	3	5.92	0.355	1.423	0.335
61902	4	8.24	0.329	1.29	0.361
63077	5	5.38	0.372	1.53	0.273
63598	6	7.94	0.366	–	0.299
76932	7	5.83	0.360	1.475	0.299
78747	8	7.73	0.383	–	0.296
79601	9	8.00	0.378	–	0.306
97320	10	8.19	0.337	1.31	0.305
111971	11	8.05	0.353	–	0.304
126793	12	8.19	0.373	1.44	0.291
134169	13	7.68	0.368	1.464	0.309
152924	14	8.02	0.318	1.24	0.379
189558	15	7.74	0.385	1.575	0.269
193901	16	8.67	0.376	1.52	0.221
194598	17	8.35	0.343	1.38	0.269
196892	18	8.24	0.346	1.37	0.307
199289	19	8.29	0.368	1.42	0.264
203608	20	4.22	0.326	1.23	0.310
215257	21	7.42	0.357	1.53	0.310

Table 2. Model parameters

HD	T_{eff} (K)	$\log g$ (cgs)	[Fe/H]	ξ (km/s)
22879	5774	4.1	−1.00	1.0
25704	5715	3.9	−1.05	1.1
59984	5860	3.8	−0.85	1.3
61902	6054	3.9	−0.85	1.3
63077	5717	4.0	−0.90	0.9
63598	5779	3.9	−0.95	1.1
76932	5798	3.9	−1.00	1.0
78747	5676	3.8	−0.80	1.0
79601	5716	3.8	−0.75	1.1
97320	6000	4.1	−1.30	1.2
111971	5880	4.0	−0.85	1.1
126793	5783	3.9	−0.90	1.3
134169	5782	3.8	−0.90	1.2
152924	6132	3.9	−0.80	1.4
189558	5628	3.8	−1.20	1.2
193901	5703	4.4	−1.15	0.8
194598	5920	4.2	−1.20	1.0
196892	5925	4.0	−1.10	1.2
199289	5808	4.1	−1.15	1.2
203608	6112	4.3	−0.80	1.3
215257	5769	3.8	−0.90	1.3

In order to find the origin of that scatter, we must improve the accuracy of the abundances. This requires both high quality data and a careful spectroscopic analysis.

Here, we report on the results of such a detailed analysis and we investigate the underlying reasons for the remaining scatter – if any. We look at correlations between different abundance ratios at a given metallicity. Strongly correlated elements are likely to have been processed in the same astrophysical sites. Therefore, the identification of such correlations can provide fruitful insights on the nucleosynthesis of these elements. This allows us to suggest a scenario for the formation of metal-poor stars. Preliminary results have already been presented briefly in Jehin et al. (1998).

2. Determination of the atmospheric parameters

3. Observations and data reduction

We have selected a sample of 21 unevolved metal-poor stars (Tables 1 and 2), with roughly one tenth of the solar metallicity ($[\text{Fe}/\text{H}] \sim -1^1$). This corresponds more or less to the transition between the halo and the disk.

The observations were carried out with the Coudé Echelle Spectrometer (CES) fed by the 1.4 m Coudé Auxiliary Telescope (CAT) at the European Southern Observatory (La Silla, Chile). The long camera was used with a Loral CCD detector (ESO #38) having 2688×512 pixels of $15 \times 15 \mu\text{m}$ each.

¹ We adopt the usual spectroscopic notation: $[\text{A}/\text{B}] \equiv \log_{10}(N_{\text{A}}/N_{\text{B}})_{*} - \log_{10}(N_{\text{A}}/N_{\text{B}})_{\odot}$ for elements A and B.

The exposure times were chosen in order to reach a signal-to-noise ratio (S/N) of at least 200 in all spectral regions. The spectra were collected during two observing runs, in January 1996 (8 nights) and July 1996 (11 nights), the last one having been carried out in remote control from the ESO headquarters in Garching bei München. All stars were observed in four wavelength bands, each band having a width of about 50\AA . These spectra are centered around 4125, 4325, 4584 and 4897\AA .

The data reduction consisted in :

1. background subtraction on the basis of the mean level measured on the parts of the CCD not illuminated by stellar light;
2. flat-fielding, using the spectrum of an internal lamp;
3. wavelength calibration, using the stellar lines themselves to define the calibration curve, thus automatically correcting for the radial velocity;
4. definition of the continuum, in the form of a low order Spline fitted through a number of pre-defined continuum windows;
5. equivalent widths (EWs) measurements, by Gaussian and Voigt function fitting, the first method being preferred for the weak lines and the second in the case of the stronger ones (for which the Lorentzian damping wings contribute significantly to the EW). The table listing the nearly 2000 EWs measurements is available in electronic form from CDS.

3.1. Effective temperature

The effective temperatures T_{eff} were determined from the Strömgren $b-y$ and Johnson $V-K$ colour indices, using the calibration of Magain (1987) which is based on the infrared flux method (Blackwell and Shallis 1977). The sources of $b-y$ measurements are Schuster and Nissen (1988), Olsen (1994) and Carney (1983). The $V-K$ colours were obtained from Carney (1983), Alonso et al. (1994) and from some unpublished measurements by P. Magain with the ESO 1 m telescope on La Silla. When several values were available for the same star, the average was taken.

The adopted effective temperature is a mean of the two determinations and is listed in Table 2. The agreement between the temperatures deduced from the two colour indices is quite good, the mean difference amounting to 45 K, with an r.m.s. scatter of 40 K in the individual determinations.

All these stars being in the solar neighbourhood (distances range from 9 to 80 pc), the interstellar reddening should be negligible. The internal precision of the effective temperatures may thus be estimated from the comparison of the two photometric determinations. The scatter of 40 K in the T_{eff} differences corresponds to an uncertainty of 28 K ($40/\sqrt{2}$) in the individual values and of 20 K in the mean T_{eff} from the two colour indices. This high internal precision can be checked from the differential excitation equilibria of FeI. The excitation equilibria indicate effective temperatures which agree quite well with the photometric values: the scatter of the excitation temperatures around the photometric ones amounts to 57 K, while the expected scatter, on the basis of a precision of 20 K on the photometric values and 45 K on the excitation values, amounts to 50 K. The 7 K difference is completely negligible and shows that the internal precision of our effective temperatures is indeed very high.

3.2. Metallicity

For the first step, the model metallicities were taken from previously published analyses. This is not a crucial parameter in metal-poor stars model atmospheres as the continuous opacity is dominated by the contribution of the negative hydrogen ion and hydrogen itself is the main electron donor. Nevertheless, the model metallicities were redetermined on the basis of our set of FeI lines. The latter values were used in the subsequent analysis.

3.3. Surface gravity

Surface gravities are usually determined by requiring FeI and FeII lines to indicate the same abundance. However, this procedure is affected by several uncertainties. For example, the iron abundance derived from FeI lines is quite sensitive to T_{eff} and unfortunately the zero-point of the

T_{eff} scale of metal-poor stars may be uncertain by as much as 100 K, causing errors in $[\text{Fe}/\text{H}]$ of about 0.10 dex and errors in the spectroscopic gravities of the order of 0.25 dex. For other uncertainties, see for e.g the discussion in Nissen et al. (1998). To avoid these problems, we decided (1) to determine the surface gravity from the Strömgren c_1 index, using the calibrations of Vandenberg and Bell (1985) for the adopted temperatures and metallicities; (2) to always derive relative abundances from the comparison of lines of the same ionization stage and, thus, of the same dependence on surface gravity.

3.4. Microturbulence velocity

Microturbulence velocities ξ are obtained, as usual, by forcing a set of lines of the same element and same ionization stage but with different EWs to indicate the same abundance. In our observations, only the FeI lines are suitable for such a determination. The precision of the microturbulence determinations, estimated by linear regression, is better than 0.1 km s^{-1} . The adopted model parameters for the 21 stars are listed in Table 2.

4. Method of analysis

4.1. A strictly differential analysis

Our stellar sample is rather homogeneous in terms of atmospheric parameters: all the stars are dwarfs or subgiants with $3.8 < \log g < 4.4$, have roughly solar temperatures with $5620 \text{ K} < T_{\text{eff}} < 6140 \text{ K}$ and a narrow range of metallicity ($-1.3 < [\text{Fe}/\text{H}] < -0.7$). A differential analysis within the sample is thus indicated, especially as we are interested in distinguishing minute variations from star to star and, so, need the highest possible internal precision.

As a first step, all stars were analysed with respect to HD 76932, one of the brightest stars in our sample, having average atmospheric parameters. The zero points of the element abundances in HD 76932 were determined from lines with laboratory gf -values (Table 3). When lines from two ionization stages were available, the abundance of the ion was forced to agree with that of the neutral.

The microturbulence velocity in the atmosphere of HD 76932, which must be known in order for this differential analysis to be carried out, was determined from a set of CaI lines with the same excitation potential, precise laboratory gf -values (Smith and Raggett 1981) and a suitable range of EWs (Table 3). These lines were observed with the same instrument in the context of another programme. A value of $\xi = 1.0 \text{ km/s}$ has been obtained.

It is possible to reduce even further the uncertainties in the relative gf -values by analysing each star with respect to each other and derive mean gf -values from the whole sample. This reduces the scatter in the line abundances for an individual star but has no effect on the mean abundances of one star relative to another, provided that

Table 3. Data for the 2.52 eV CaI lines in HD 76932: wavelength λ , excitation potential χ , oscillator strength $\log gf$, equivalent width EW and damping enhancement factor f_6 over the Unsöld formula.

λ (Å)	χ (eV)	$\log gf$	EW (mÅ)	f_6
5260.390	2.52	-1.719	8.6	1.4
5261.710	2.52	-0.579	54.2	1.4
6161.295	2.52	-1.266	23.4	2.0
6163.754	2.52	-1.286	25.3	2.0
6166.440	2.52	-1.142	29.1	2.0
6169.044	2.52	-0.797	49.9	2.0
6169.564	2.52	-0.478	66.3	2.0
6493.788	2.52	-0.109	83.4	0.8
6499.654	2.52	-0.818	47.9	0.8

exactly the same lines are used in both stars. Since this is not the case for all stars, we only used this global differential analysis whenever justified, i.e. when the number of lines of a given species is large enough and when the line sample varies from star to star. Such an analysis was performed for FeI, FeII, TiI, TiII, CrI, CrII and NiI.

4.2. Model atmospheres and line analysis

The abundance analysis was carried out with model atmospheres constructed individually for each star. The usual assumptions of Local Thermodynamic Equilibrium (LTE) and plane parallel (horizontally homogeneous) atmospheres were made. These models were calculated on the basis of the temperature stratifications ($T(\tau)$ relations) of Kurucz (1993). Given the $T(\tau)$ relation, the gas pressure, the electron pressure and the continuous absorption were computed with a programme based on the Gustafsson et al. (1975) subroutines.

When more than one line of the same species was measured for a star, the mean abundance value and the standard deviation were computed. Whenever possible, the analysis was restricted to lines having EWs between 5 and 50 mÅ. Using weaker lines would lead to increased random errors (and possibly some systematic overestimates), while stronger lines are very sensitive to microturbulence and damping. In a few cases, however, especially for Mg, rather strong lines had to be used, while only very weak lines were available for Zr, Sm and Ce. The damping constants γ were computed with the Unsöld formula (Gray 1972), with an empirical enhancement factor of 1.5.

The 93 spectral lines used in the abundance analysis are listed in Table 4. They were selected after a careful inspection of the stellar and solar spectra. The lines were chosen as far as possible to be free of blends affecting the EW measurements.

5. Element abundances

Table 4. Atomic line data

The six columns give, respectively, the element and its ionization stage, the wavelength, the excitation potential of the lower level, the differential $\log gf$ determined from our analysis, the absolute $\log gf$ from the literature and the EW in the spectrum of HD 76932.

El.	λ (Å)	χ (eV)	$\log gf$ dif.	$\log gf$ abs.	HD 76932 (mÅ)
Mg I	4571.102	0.00	-5.014	-5.550	76.0
Ca I	4108.532	2.71	-0.547		31.9
Ca I	4578.559	2.52	-0.415	-0.697	48.5
Sc II	4314.091	0.62	0.378	-0.040	98.1
Sc II	4320.749	0.61	0.147	-0.210	87.8
Ti I	4112.716	0.05	-1.648	-1.758	13.9
Ti I	4870.136	2.25	0.501	+0.358	16.0
Ti I	4885.088	1.89	0.497		29.0
Ti I	4913.622	1.87	0.267	+0.160	20.7
Ti II	4316.802	2.05	-1.498		34.2
Ti II	4330.245	2.05	-1.552		32.7
Ti II	4330.708	1.18	-1.892		53.8
Ti II	4563.766	1.22	-0.599		105.4
Ti II	4568.328	1.22	-2.752		17.6
Ti II	4571.982	1.57	-0.100		124.0
Ti II	4583.415	1.16	-2.739		19.6
Ti II	4589.953	1.24	-1.446		70.4
Ti II	4874.014	3.09	-0.809		22.5
Ti II	4911.199	3.12	-0.493		34.7
V I	4111.787	0.30	-0.047	+0.408	42.6
V I	4115.177	0.29	-0.407	+0.071	28.1
V I	4330.024	0.00	-1.148	-0.631	13.7
V I	4577.184	0.00	-1.618	-1.048	5.6
V I	4594.126	0.07	-1.232	-0.672	10.7
V I	4875.492	0.04	-1.355	-0.807	9.3
Cr I	4111.358	2.90	-0.442		11.5
Cr I	4129.184	2.91	+0.246		35.4
Cr I	4580.062	0.94	-1.580		38.2
Cr I	4600.757	1.00	-1.376	-1.276	43.5
Cr I	4870.816	3.08	+0.162		25.8
Cr I	4885.774	2.54	-2.117	-1.055	5.5
Cr II	4558.650	4.07	-0.465		55.5
Cr II	4588.204	4.07	-0.686		47.2
Cr II	4592.057	4.07	-1.293		23.5
Cr II	4884.598	3.86	-2.083		9.0
Fe I	4109.062	3.29	-1.464		36.0
Fe I	4112.323	3.40	-1.701		20.1
Fe I	4114.451	2.83	-1.366		56.5
Fe I	4114.942	3.37	-1.644		22.8
Fe I	4120.212	2.99	-1.290		53.8
Fe I	4124.489	3.64	-2.219		4.7
Fe I	4125.886	2.84	-2.056		28.3
Fe I	4126.191	3.33	-0.963		57.5
Fe I	4126.857	2.84	-2.763		7.8
Fe I	4132.908	2.84	-0.997	-0.960	71.0
Fe I	4136.527	3.37	-1.573		25.1
Fe I	4137.005	3.41	-0.670		62.2

Table 4. Atomic line data (contd.)

El.	λ (Å)	χ (eV)	$\log gf$ dif.	$\log gf$ abs.	HD 76932 (mÅ)
Fe I	4137.415	4.28	-0.961		17.4
Fe I	4566.524	3.30	-2.228		10.7:
Fe I	4574.225	3.21	-2.419		8.4
Fe I	4574.728	2.28	-2.889		18.3
Fe I	4587.134	3.57	-1.727		14.7
Fe I	4595.365	3.30	-1.712		26.6
Fe I	4596.416	3.65	-2.169		6.0
Fe I	4598.125	3.28	-1.529		34.2
Fe I	4602.008	1.61	-3.182	-3.154	30.2
Fe I	4602.949	1.48	-2.195	-2.220	76.0
Fe I	4875.881	3.33	-1.900		18.2
Fe I	4885.434	3.88	-1.045		30.3
Fe I	4886.337	4.15	-0.735		33.4
Fe I	4896.442	3.88	-1.931		6.2
Fe I	4907.735	3.43	-1.804		18.3
Fe I	4908.032	4.22	-1.562		7.4
Fe I	4910.020	3.40	-1.348		38.5
Fe I	4910.330	4.19	-0.742		30.0
Fe I	4910.570	4.22	-0.754		31.4
Fe I	4911.782	3.93	-1.687		9.0
Fe I	4917.235	4.19	-1.025		19.9
Fe I	4918.015	4.23	-1.212		14.4:
Fe II	4128.742	2.58	-3.668		24.4
Fe II	4576.339	2.84	-3.047		41.0
Fe II	4582.833	2.84	-3.280		30.8
Ni I	4331.651	1.68	-2.146	-2.100	31.6
Ni I	4600.364	3.60	-0.499		24.2
Ni I	4604.996	3.48	-0.252	-0.250	38.4
Ni I	4606.226	3.60	-0.921		11.3:
Ni I	4873.446	3.70	-0.459	-0.380	22.1
Ni I	4904.418	3.54	-0.079		45.0
Ni I	4912.025	3.77	-0.739		12.4
Ni I	4913.978	3.74	-0.569		17.3
Ni I	4918.371	3.84	-0.140		29.9
Sr I	4607.338	0.00		0.280	14.9
Y II	4883.690	1.08	+0.074	0.070	42.3
Y II	4900.124	1.03	-0.072	-0.090	38.7
Zr II	4317.321	0.71		-1.380	8.3
Ba II	4130.657	2.72		0.560	18.8
La II	4322.505	0.17	-0.938		5.4
La II	4333.763	0.17	-0.152	-0.160	22.4
Ce II	4137.655	0.52	+0.065		10.2
Ce II	4562.367	0.48	-0.080	0.330	9.1
Nd,II	4109.450	0.32	+0.548	0.519	20.0
Nd II	4314.512	0.00	-0.292	-0.226	8.4
Sm II	4318.936	0.28		-0.270	6.4
Eu II	4129.724	0.00		0.204	38.8

5.1. Iron peak elements

We have obtained the abundances of four iron peak elements, namely V, Cr, Fe and Ni (Table 5). They all have a rather large number of clean lines and the line-to-line scatter of the abundances is small ($\langle \sigma \rangle \sim 0.03$). In the case of Fe and Cr, both neutral and ionized lines are available.

Our iron abundances are based on 34 FeI and 3 FeII transitions. The zero point for iron was obtained from 3 FeI lines with accurate oscillator strengths from the Oxford group (Blackwell et al. 1982a and references therein). The iron ionization equilibrium is satisfied to a good accuracy ($\langle [\text{Fe}/\text{H}]_{\text{I}} - [\text{Fe}/\text{H}]_{\text{II}} \rangle = +0.011 \pm 0.051$), the small scatter confirming the photometrically determined surface gravities.

From the 6 CrI and 4 CrII lines available in our spectra, we find that the chromium abundance in metal-poor stars scales like the iron one. The scatter around the mean is very small in both cases: 0.030 dex for $[\text{Cr}/\text{Fe}]_{\text{I}}$ and 0.032 dex for $[\text{Cr}/\text{Fe}]_{\text{II}}$. The agreement between the neutral and ionized lines is satisfactory: $\langle [\text{Cr}/\text{H}]_{\text{I}} - [\text{Cr}/\text{H}]_{\text{II}} \rangle = +0.002 \pm 0.050$. The zero point was fixed from the oscillator strengths of Blackwell et al. (1984, 1986b) for CrI.

Nickel is represented in our spectra by 9 clean NiI lines. The three absolute $\log gf$ available for the zero point calibration are from Doerr and Kock (1985) and the recent determinations from Wickliffe and Lawler (1997).

Because of the lack of hyperfine structure (HFS) data for our VI lines, we have restricted our analysis to 6 lines with EWs smaller than 30 mÅ (except 4111.787 Å which is slightly stronger but had to be included for our most metal-poor stars). Using accurate transition probabilities from Whaling et al. (1985) we have derived gf -values for each VI line. Absolute abundances were thus computed and compared with the results obtained from the differential analysis. The very small scatter around the mean difference ($\langle \sigma \rangle \sim 0.02$) reflects the high internal accuracy of the two sets of gf -values. The relative abundances of iron peak elements are listed in Table 5.

5.2. α elements

The magnesium abundance is obtained from a single MgI line, the calcium abundance from two neutral lines and the titanium abundance from a first set of 4 TiI lines and a second set of 8 TiII lines.

Only the rather strong intercombination MgI line (~ 70 mÅ) at 4571 Å is available in our spectra for the Mg abundance determination. The deduced abundance is thus more sensitive to the microturbulence velocity ξ .

The line-to-line scatter in the deduced titanium abundances is ~ 0.025 . The ionization equilibrium of titanium confirms, once again, the validity of the photometric surface gravities: $\langle [\text{Ti}/\text{H}]_{\text{I}} - [\text{Ti}/\text{H}]_{\text{II}} \rangle = +0.016 \pm 0.044$. The

Table 5. Iron peak element abundances and line-to-line scatter

ID	[Fe/H] _I	[Fe/H] _{II}	[V/Fe] _I	[Cr/Fe] _I	[Cr/Fe] _{II}	[Ni/Fe] _I
1	-0.892(16)	-0.888(12)	-0.032(36)	-0.111(28)	-0.107(26)	-0.082(32)
2	-0.960(26)	-1.001(19)	0.015(33)	-0.124(33)	-0.109(30)	-0.093(37)
3	-0.755(27)	-0.755(07)	-0.103(32)	-0.098(43)	-0.128(15)	-0.112(33)
4	-0.727(23)	-0.693(16)	-0.102(36)	-0.098(51)	-0.130(49)	-0.122(29)
5	-0.831(22)	-0.840(10)	0.030(35)	-0.079(38)	-0.052(56)	-0.070(33)
6	-0.856(27)	-0.970(25)	-0.046(66)	-0.101(41)	-0.099(41)	-0.086(36)
7	-0.910(29)	-0.910(12)	-0.039(37)	-0.089(35)	-0.089(22)	-0.083(31)
8	-0.730(20)	-0.857(11)	-0.033(34)	-0.098(55)	-0.070(17)	-0.084(32)
9	-0.668(23)	-0.760(17)	0.008(29)	-0.072(26)	-0.023(24)	-0.074(31)
10	-1.220(17)	-1.179(31)	-0.095(82)	-0.124(32)	-0.108(46)	-0.080(35)
11	-0.737(27)	-0.748(25)	-0.136(30)	-0.157(56)	-0.105(33)	-0.134(30)
12	-0.800(24)	-0.864(17)	-0.001(55)	-0.113(47)	-0.117(31)	-0.080(30)
13	-0.804(32)	-0.823(10)	-0.069(37)	-0.107(43)	-0.086(15)	-0.095(46)
14	-0.708(28)	-0.675(41)	-0.106(140)	-0.088(62)	-0.102(49)	-0.082(32)
15	-1.129(34)	-1.093(30)	-0.037(38)	-0.098(51)	-0.132(40)	-0.108(38)
16	-1.071(25)	-1.043(06)	-0.200(58)	-0.154(38)	-0.143(31)	-0.232(44)
17	-1.126(30)	-1.074(28)	-0.139(57)	-0.164(33)	-0.141(76)	-0.185(45)
18	-1.031(21)	-1.025(13)	-0.024(81)	-0.082(45)	-0.064(33)	-0.077(37)
19	-1.074(32)	-1.100(18)	-0.023(63)	-0.142(45)	-0.065(48)	-0.055(39)
20	-0.677(29)	-0.636(07)	-0.079(51)	-0.109(93)	-0.133(30)	-0.086(37)
21	-0.804(29)	-0.814(15)	-0.160(90)	-0.162(36)	-0.088(39)	-0.136(43)

Table 6. α element abundances and line-to-line scatter

ID	[Mg/Fe] _I	[Ca/Fe] _I	[Ti/Fe] _I	[Ti/Fe] _{II}
1	0.344	0.197(37)	0.249(20)	0.234(22)
2	0.269	0.133(82)	0.217(74)	0.180(46)
3	0.239	0.065(39)	0.105(32)	0.126(27)
4	0.077	0.050(59)	0.102(32)	0.077(21)
5	0.344	0.175(27)	0.230(46)	0.264(22)
6	0.299	0.185(37)	0.260(29)	0.258(35)
7	0.366	0.242	0.241(31)	0.241(21)
8	0.322	0.260(24)	0.233(32)	0.271(38)
9	*	0.198(24)	0.227(25)	0.251(23)
10	0.303	0.169(55)	0.260(20)	0.217(57)
11	0.096	0.054(47)	0.058(30)	0.048(29)
12	0.341	0.185(27)	0.244(28)	0.263(23)
13	0.326	0.152(86)	0.182(39)	0.186(14)
14	0.234	0.132(88)	0.173(44)	0.172(49)
15	0.398	0.242(42)	0.256(62)	0.234(34)
16	0.164	0.119(60)	0.071(38)	0.101(34)
17	0.139	0.177	0.120(52)	0.091(43)
18	0.324	0.222(39)	0.272(29)	0.251(31)
19	0.338	0.167(46)	0.262(40)	0.235(20)
20	0.152	-0.007(60)	0.072(35)	0.029(23)
21	0.063	0.084(33)	0.033(44)	0.032(27)

zero point was determined from 3 accurate TiI gf -values (Blackwell et al. 1982b, 1986a).

The relative abundances are given in Table 6.

5.3. Heavy elements

For the sake of clarity, we shall distinguish between the light s -process elements (Sr, Y, Zr), the heavy s -process

elements (Ba, La, Ce) and the mixed or r -process elements (Nd, Sm, Eu). This is of course an oversimplification, several processes contributing in variable proportions to the synthesis of each of them.

For Sr, we used the neutral resonance line at 4607.34 Å with an oscillator strength $\log gf = 1.92 \pm 0.06$ (Migdalek and Baylis (1987)), a value which is in agreement with both experimental and theoretical determinations.

The agreement between our two lines of YII is always very good, with a mean difference of 0.02 between the two line abundances. The absolute $\log gf$ used were determined from measurements of radiative lifetimes and branching ratios (Hannaford et al. 1982).

The only ZrII line available in our spectra has an accurate laboratory oscillator strength (Biémont et al. 1981).

The only Ba line available is the 4130 Å BaII line. The abundances were computed with 9 HFS components but the HFS effect turns out to be very small. The transition probability was taken from Gallagher (1967). This line is slightly blended on the red wing with a CeII line but the error on the deduced differential abundances should not exceed 5%.

For the LaII line at 4333 Å, we have adopted the transition probability calculated by Gratton and Sneden (1991) from the experimental lifetime measurements of Arnesen et al. (1977a, 1977b) and Andersen et al. (1975). No HFS was included because the EWs never exceed 30 mÅ. This line is slightly blended by a CH line but no correction was applied.

Two lines of CeII are measurable in our spectra but are located in very crowded regions. Moreover, these two

Table 7. Heavy element abundances and line-to-line scatter

ID	[Sr/Fe]I	[Y/Fe]II	[Zr/Fe]II	[Ba/Fe]II	[La/Fe]II	[Ce/Fe]II	[Nd/Fe]II	[Sm/Fe]II	[Eu/Fe]II
1	-0.099	-0.033(13)	0.155	0.180	0.241(39)	0.007(13)	-0.103(21)	0.208	0.188
2	-0.119	-0.174(19)	-0.009	0.078	0.141(104)	-0.105(31)	-0.055	0.170	0.161
3	-0.231	-0.195(09)	-0.020	0.048	0.120	-0.125	-0.190(18)	0.017	0.080
4	-0.236	-0.264(32)	-0.027	-0.005	0.067(26)	-0.165(16)	-0.251	0.007	-0.007
5	-0.127	-0.070(19)	0.084	0.092	0.220(13)	-0.134	-0.114(51)	0.164	0.195
6	-0.145	0.005(54)	0.195	0.145	0.200(80)	-0.104(39)	-0.093(33)	0.287	0.205
7	-0.086	0.045(15)	0.190	0.119	0.198	-0.050	-0.098	0.242	0.210
8	-0.170	-0.050(19)	0.159	0.109	0.208	-0.064	-0.064(60)	0.187	0.162
9	-0.233	-0.151(21)	0.054	0.055	0.147	-0.165(63)	-0.073(19)	0.218	0.185
10	0.003	-0.150(34)	*	0.060	0.100	-0.189	0.046	0.267	0.229
11	-0.314	-0.218(32)	-0.153	0.026	0.126	-0.074	-0.258(27)	-0.126	-0.027
12	-0.118	-0.102(20)	0.174	0.141	0.258	-0.067(39)	-0.136(25)	0.191	0.184
13	-0.276	-0.193(39)	0.027	0.057	0.117(61)	-0.104(45)	-0.202(15)	0.051	0.148
14	-0.279	-0.196(48)	-0.070	-0.086	0.072(62)	-0.167	-0.293	-0.022	0.135
15	0.002	0.117(31)	0.363	0.396	0.338(95)	0.112(66)	-0.033(54)	0.229	0.223
16	-0.383	-0.207(49)	*	0.147	0.288	0.076	-0.016	0.374	0.363
17	-0.351	-0.230(31)	-0.106	-0.015	0.175	-0.023	-0.025	0.283	0.214
18	-0.103	0.048	0.353	0.155	0.275(16)	0.056(28)	-0.104(25)	0.313	0.200
19	-0.198	-0.138(35)	0.109	0.038	0.276(134)	0.008(111)	*	0.117	0.185
20	-0.254	-0.223(20)	-0.032	0.038	0.135(22)	-0.045(20)	-0.203(07)	0.149	0.026
21	-0.329	-0.309(16)	-0.095	0.054	0.079(33)	-0.123	-0.286	0.016	-0.006

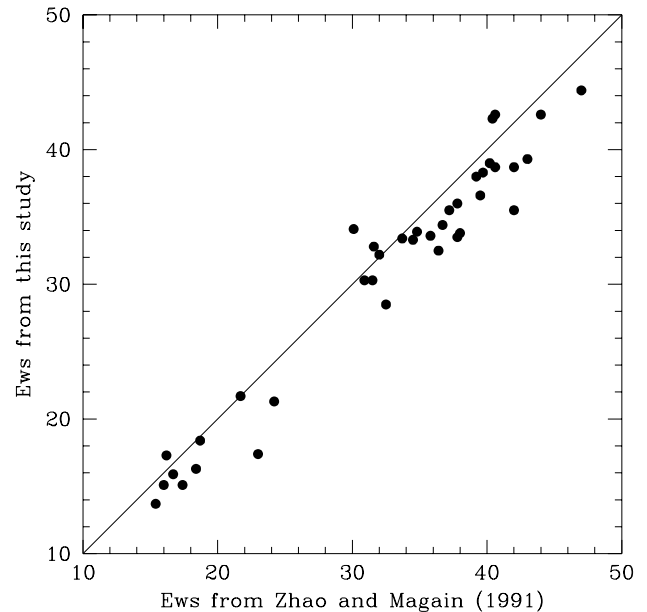
lines are not available for all the stars. For the zero point, we have adopted the transition probability given by Gratton and Sneden (1991) for the 4562 Å line, determined by renormalizing the values of Corliss and Bozman (1962) to the lifetimes results of Andersen et al. (1975). The abundance derived for HD 97320 is very uncertain.

The NdII lines are also not easy to measure and are not available for all stars. We have performed an inverse solar analysis to obtain $\log gf$ values, but the zero point is somewhat uncertain.

The Sm abundance was derived from a single weak SmII line, and the zero point deduced from the oscillator strength given by Biémont et al. (1989).

The EuII line at 4129.724 Å has both a large HFS and a significant isotopic shift. Each of the two isotopes has 16 HFS components (Woolf et al. 1995). They were all included, based on the data from Broström et al. (1995) for the isotopic shift (4578 MHz). The 32 HFS components were calculated using data from Becker et al. (1983), Villamoës and Wang (1994) and Möller et al. (1993). A laboratory gf -value ($\log gf = 0.204 \pm 0.027$), determined from lifetimes and relative line intensities (Biémont et al. 1982) was used. The isotopic ratio was assumed to be identical to the meteoritic value. For each star we have computed synthetic spectra between 4129.5 and 4130.1 Å including also 5 FeI lines with $\log gf$ from Grevesse and Sauval (private communication). The macroturbulence velocities were determined from a set of 5 clean FeI lines in this spectral window. The Eu abundance was adjusted until the synthetic and observed spectra matched.

The abundances of the neutron capture elements relative to Fe are given in Table 7.

**Fig. 1.** Comparison of our EWs with those measured by Zhao and Magain (1991)

6. Estimation of the uncertainties

We now discuss the uncertainties on the abundances. First, we consider the errors which act on single lines and, secondly, those which affect whole sets of lines.

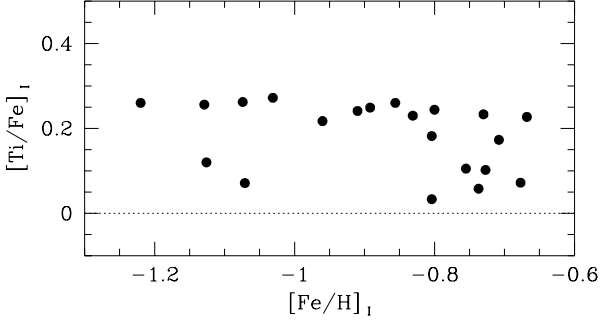


Fig. 2. Traditional plot: the abundance of Ti relative to Fe versus $[\text{Fe}/\text{H}]$

In the first category, we have the uncertainties on the line parameters, i.e., the random errors on EWs, on oscillator strengths, on damping constants,...

They can be estimated by comparing the results from different lines of the same element. With 30 Fe I lines ($5 \text{ mÅ} < \text{EW} < 70 \text{ mÅ}$), the scatter varies somewhat from star to star (from 0.016 to 0.034) with a mean value of 0.027 dex. We find similar values for other elements having a significant number of lines in our spectra (Ni I, Ti II, ...).

Our EW measurements for the 10 stars which also appear in Zhao and Magain (1991) are plotted in Fig. 1. The small systematic difference is due to a non-linearity of the CCD used by Zhao and Magain, which accounts for an overestimate of about 5% in their EWs (Gosset and Magain 1993). Apart from that, the agreement is very good, with a scatter of 1.5 mÅ only. Thus, if the two studies were of the same quality, the precision on the EWs would be 1 mÅ . For typical lines having EWs of 25 mÅ the corresponding error on the abundance is of the order of 0.02 dex.

Considering these two different estimates (0.027 and 0.02 dex), the total abundance error coming from EW measurements can be assumed to amount to $0.025/\sqrt{N}$, where N is the number of lines measured.

The second category of errors are essentially model errors, such as uncertainties on the effective temperature, surface gravity, microturbulence velocity, overall metallicity and temperature structure. We estimate uncertainties in the differential T_{eff} values due to errors in observed photometric indices to be about 20 K (see Section 3.1). In $\log g$ the total errors may approach 0.2 dex, resulting from errors in the c_1 index, and uncertainties in the calibration of Vandenberg and Bell (1985). If there is a systematic error in T_{eff} , it will affect our $\log g$ determination. However, the three ionization equilibria available confirm the differential photometric gravities (Sections 5.1 and 5.2). A systematic error on all surface gravities will not change the abundance ratios. Moreover, the comparison with the “Hipparcos parallax-based gravities” of Nissen et al. (1998) for the four stars in common shows that,

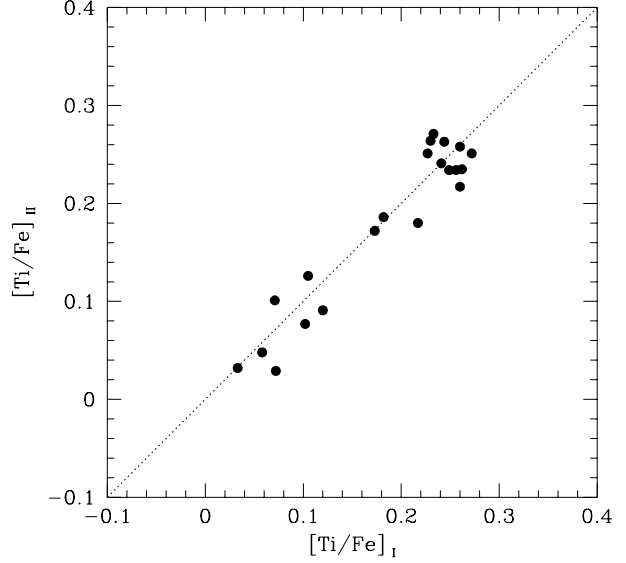


Fig. 3. Comparison of the values of $[\text{Ti}/\text{Fe}]$ determined from ionic and from neutral lines

Table 8. Influence of errors in the model parameters on the HD 199289 abundances

Element abundance	ΔT_{eff} +20K	$\Delta \log g$ +0.2	$\Delta [\text{Fe}/\text{H}]$ +0.2	$\Delta \xi$ +0.1	Rms sum
[Fe/H] I	+0.014	+0.010	−0.001	−0.009	0.019
[Fe/H] II	+0.002	+0.090	+0.014	−0.008	0.091
[Cr/Fe] I	+0.002	+0.002	+0.003	+0.002	0.005
[Cr/Fe] II	−0.003	+0.002	−0.005	−0.004	0.007
[Ti/Fe] I	+0.002	−0.003	+0.002	+0.006	0.007
[Ti/Fe] II	+0.000	−0.003	−0.005	−0.010	0.012
[Mg/Fe] I	+0.010	+0.020	−0.007	−0.012	0.026
[Ca/Fe] I	−0.003	−0.007	+0.004	+0.005	0.010
[V/Fe] I	+0.007	−0.005	+0.002	+0.009	0.013
[Ni/Fe] I	−0.001	+0.004	+0.001	+0.002	0.005
[Sr/Fe] I	+0.003	−0.003	+0.000	+0.005	0.007
[Y/Fe] II	+0.006	+0.004	+0.005	−0.002	0.009
[Zr/Fe] II	+0.007	−0.012	+0.008	+0.007	0.017
[Ba/Fe] II	+0.001	−0.009	+0.000	+0.003	0.010
[La/Fe] II	+0.008	+0.000	+0.009	+0.003	0.012
[Ce/Fe] II	+0.009	−0.008	+0.011	+0.006	0.017
[Nd/Fe] II	+0.008	−0.013	+0.017	+0.004	0.023
[Sm/Fe] II	+0.009	−0.012	+0.011	+0.007	0.020
[Eu/Fe] II	+0.009	−0.025	+0.011	+0.003	0.029

if present, such a systematic error is very small, of the order of 0.12 ± 0.03 dex.

The variations of the abundance ratios due to changes on effective temperature (+20K), surface gravity (+0.2 dex), model metallicity (+0.2 dex) and microturbulence velocity (+0.1 dex) are summarized in Table 8 for a typical star. The total uncertainty never exceeds some 10% for all abundance ratios.

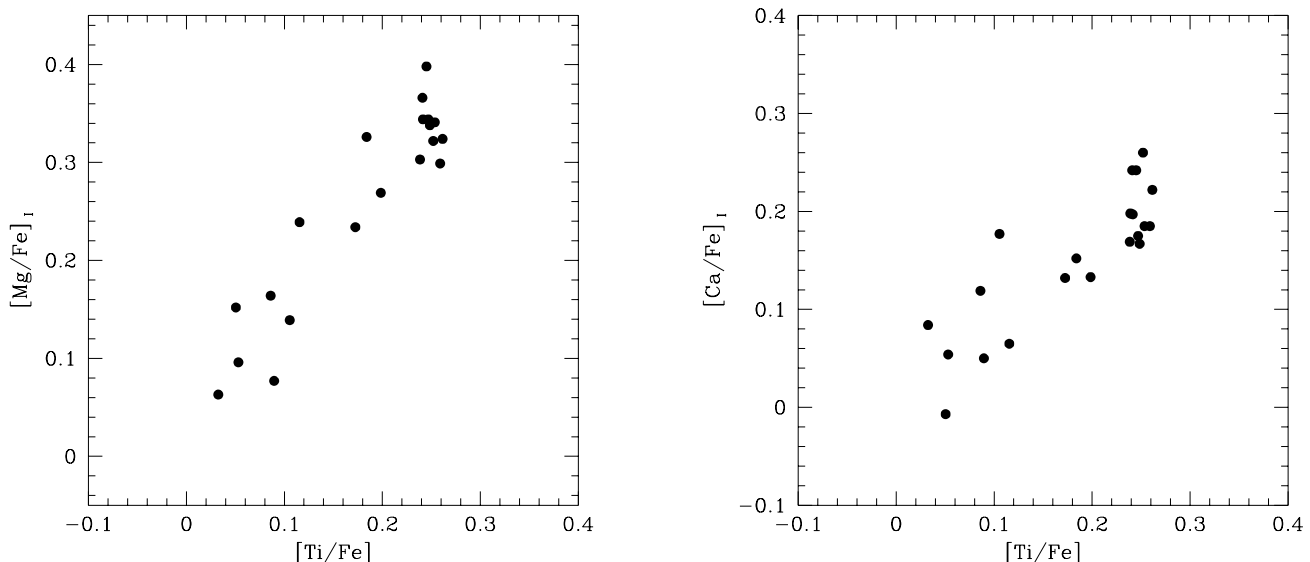


Fig. 4. Correlation diagrams for $[\text{Mg}/\text{Fe}]$ and $[\text{Ca}/\text{Fe}]$ versus $[\text{Ti}/\text{Fe}]$

In Fig. 2, we show the abundance of titanium relative to iron as deduced from the neutral lines versus $[\text{Fe}/\text{H}]$. It appears that the scatter in $[\text{Ti}/\text{Fe}]$, which amounts to 0.08 dex, is much larger than the estimated error on that abundance ratio (0.013). It seems therefore that the observed scatter is not due to analysis uncertainties and could be genuine cosmic scatter.

We confirm this result by comparing the values of $[\text{Ti}/\text{Fe}]$ deduced from neutral lines with those obtained from the ionized lines, as shown in Fig. 3. We see that the correlation between the two ratios is close to perfect, the remaining scatter amounting to 0.025 dex only, which is compatible with the estimated errors (0.024 dex). These two determinations of $[\text{Ti}/\text{Fe}]$ are completely independent since the sensitivity of the ionic lines to errors on the model parameters is different from that of the neutral lines.

We conclude that the observed scatter is indeed of cosmic origin and that the high precision of our results allows us to investigate the correlations between different relative abundances.

7. Abundance correlations

7.1. α elements

In Fig. 4 we show the abundance of Mg relative to Fe, $[\text{Mg}/\text{Fe}]$, as a function of $[\text{Ti}/\text{Fe}]$, and $[\text{Ca}/\text{Fe}]$ versus $[\text{Ti}/\text{Fe}]$. These two figures show that the three α -elements Mg, Ca and Ti behave in the same way, which means that they were synthesized by the same nucleosynthetic process in similar objects. This is in agreement with the generally accepted view that the α -elements are mainly produced in supernova explosions of massive stars (Ar-

nett 1991, Thielemann et al. 1993, Woosley and Weaver 1995).

7.2. Iron peak elements

The abundances of Cr and Fe relative to Ti are displayed in Fig. 5. The correlation is very good, with a scatter of only 0.023 dex. The second part of the same figure shows the same comparison for Ni and Fe. Here again, the correlation is remarkable ($\sigma = 0.013$) for all but two stars, which appear to be somewhat depleted in nickel. These two stars, which also display other abundance anomalies (as we shall see below) are identified by open symbols in this figure and the following ones.

While the even iron peak elements correlate very well with each other, the situation appears different for the odd element vanadium. As shown in Fig. 6, the vanadium abundance does not correlate well with the other iron peak ones. The correlation is only slightly better with the α -elements. It is difficult to draw any conclusion without investigating the behaviour of the other odd iron peak elements Mn and Co.

7.3. Neutron capture elements

We wanted to carry out the same analysis for the neutron capture elements, in order to distinguish between the s and r processes at an early stage of the galactic evolution, and to identify the most likely sites for their formation. A correlation plot for a typical s element, yttrium, is shown in Fig. 7, together with the corresponding diagram for the r element europium. The difference between the behaviours of Y and Eu is striking. Apart for the two “anomalous” stars, there is a one-to-one correlation be-

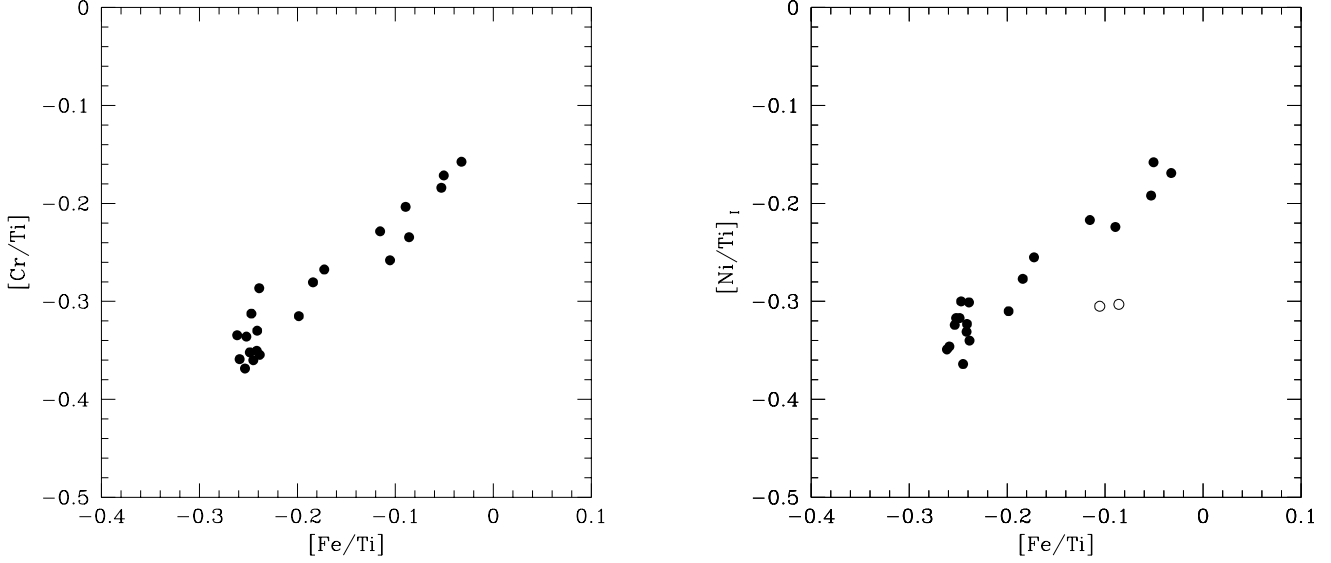


Fig. 5. Correlation diagrams for $[\text{Cr}/\text{Ti}]$ and $[\text{Ni}/\text{Ti}]$ versus $[\text{Fe}/\text{Ti}]$

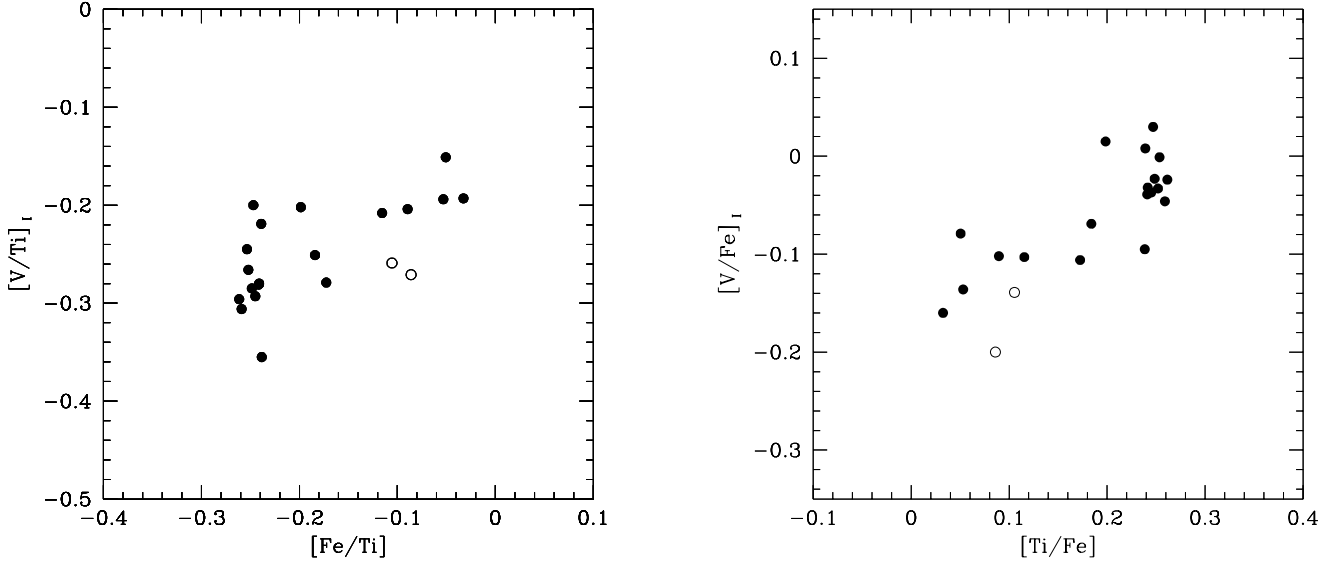


Fig. 6. Correlation diagrams for $[\text{V}/\text{Ti}]$ versus $[\text{Fe}/\text{Ti}]$ and $[\text{V}/\text{Fe}]$ versus $[\text{Ti}/\text{Fe}]$

tween the r -process element Eu and the α -element Ti. All points are located on a single straight line with a slope close to 1 and ending with a clumping at the maximum value of $[\text{Ti}/\text{Fe}]$.

In contrast, the diagram of the s -process element Y is much more complex. Here, we do not have a simple correlation with the α -elements, but rather, two distinct behaviours. For about half of the stars, corresponding to low values of $[\text{Ti}/\text{Fe}]$, there is a correlation between $[\text{Y}/\text{Fe}]$ and $[\text{Ti}/\text{Fe}]$, but the slope is significantly smaller than 1.

The remaining stars have a constant (and maximum) $[\text{Ti}/\text{Fe}]$ and increasing values of $[\text{Y}/\text{Fe}]$, starting at the

maximum value reached by the first group. We refer to such an abundance correlation as a *two branches diagram*.

Such a strikingly different behaviour needs to be confirmed by other r and s elements. Figure 8 shows the same correlation diagram for the other light s -process elements Sr and Zr, which agree very well with the diagram for Y, although the Sr and Zr results are based on the analysis of a single line, which is moreover very weak in the case of Zr. The three light s -process elements Sr, Y and Zr thus show a common pattern. We propose an explanation for these *two branches diagrams* in Section 9.

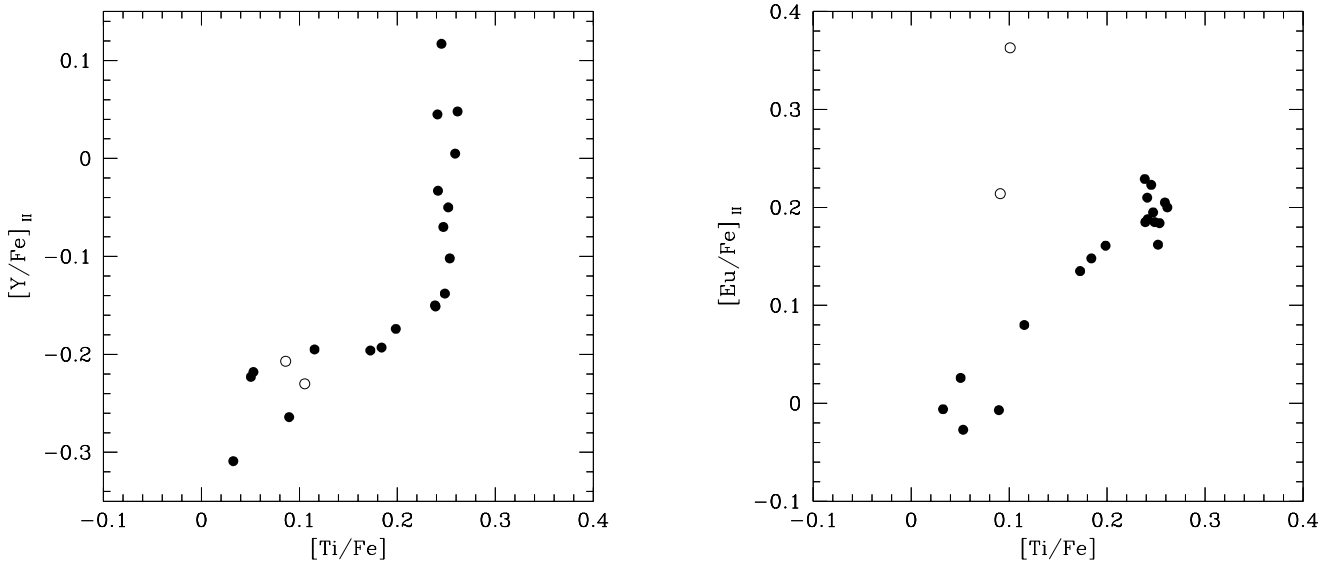


Fig. 7. Correlation diagrams for $[Y/Fe]$ and $[Eu/Fe]$ versus $[Ti/Fe]$

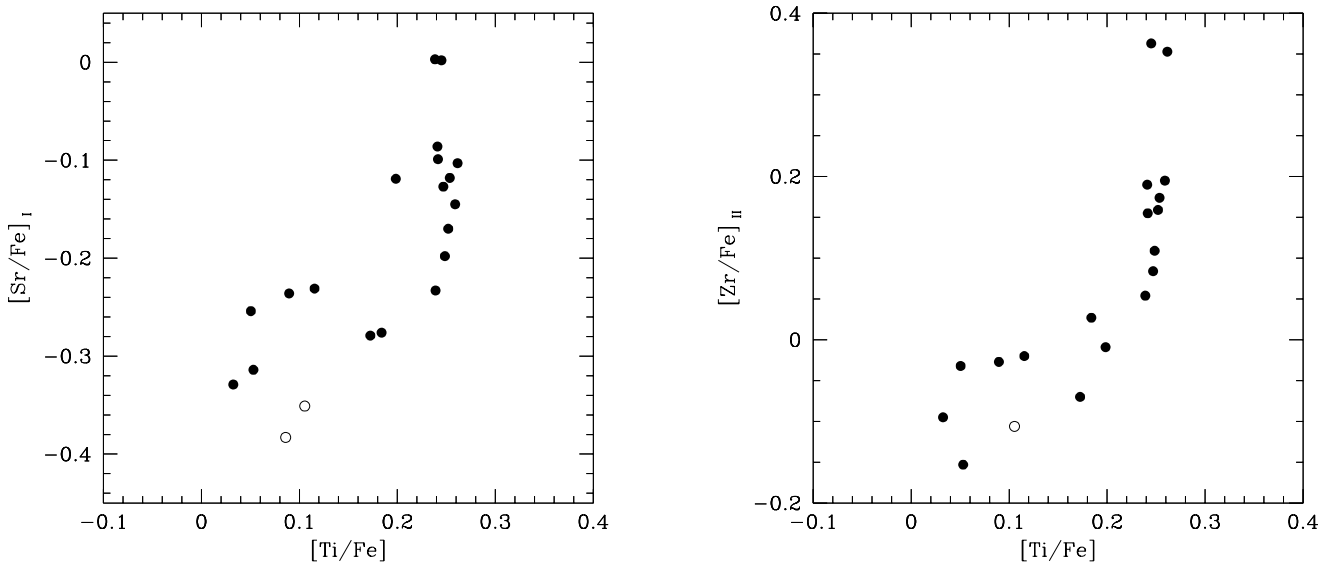


Fig. 8. Correlation diagrams for $[Sr/Fe]$ and $[Zr/Fe]$ versus $[Ti/Fe]$

The heavy s -process elements Ba, La and Ce have been considered together in Fig. 9 since the available spectroscopic data were of slightly lower quality. Despite the larger scatter, these elements all follow the same trend. Once again, we can distinguish two groups of stars, the first one with variable $[Ti/Fe]$ and a second vertical one at the maximum value of this abundance ratio.

The slope for the first group of stars is not as well defined as in the case of the lighter s elements. This may be due to the lower quality of the data, but might also reflect a different nucleosynthetic history. The latter hypothesis is supported by the fact that at least one of the anomalous

stars, which perfectly fits in the light s diagrams, now shows up again as overenriched in heavier s elements.

The cases of Nd and Sm are illustrated in Fig. 10. These elements, formed by both neutron capture processes in the solar system, display a pattern intermediate between those of the r -process element Eu and the heavy s -process ones. For low values of $[Ti/Fe]$, $[Nd/Fe]$ and $[Sm/Fe]$ are roughly constant, except for the two anomalous stars, which are relatively enriched. Near the maximum value of $[Ti/Fe]$, a looser clumping appears, with a dispersion which is intermediate between those of the r and s elements.

Table 9. Kinematic data. Radial velocity v_R , parallax π , proper motion in right ascension μ_α and in declination μ_δ , and the deduced galactic velocity components with respect to the LSR: U, V, W. (U is positive towards the galactic anticentre)

ID	v_R (km/s)	π (mas)	μ_α (mas/yr)	μ_δ (mas/yr)	U (km/s)	V (km/s)	W (km/s)
1	118.0	41.07	689.67	-214.34	98.36	-70.97	-37.11
2	52.0	19.02	347.27	413.51	118.63	-49.50	1.44
3	57.4	33.40	-92.20	-167.52	19.33	-36.24	-10.81
4	-1.0	12.01	-12.86	-201.75	-80.07	17.71	-31.50
5	102.6	65.79	-220.83	1722.89	135.33	-43.40	46.89
6	62.0	20.14	152.49	-239.09	-39.46	-71.50	9.89
7	120.8	46.90	244.35	213.46	38.23	-76.80	77.39
8	-1.0	25.16	-64.62	-132.59	-20.41	16.88	-18.56
9	32.0	18.66	-157.82	-56.85	9.35	-18.72	-29.12
10	51.1	17.77	159.19	-201.28	-83.37	-5.22	-30.28
11	-10.0	15.34	-45.01	79.26	7.83	17.55	30.87
12	-9.0	17.71	-12.45	-64.29	2.99	15.15	-7.15
13	28.5	16.80	0.71	-14.74	-26.66	12.72	22.12
14	31.0	13.72	-63.25	17.68	-34.98	-11.53	20.66
15	-14.7	14.76	-309.16	-365.29	-84.12	-113.76	50.62
16	-172.0	22.88	539.73	-1055.93	145.69	-230.16	-66.03
17	-247.0	17.94	117.90	-549.71	66.11	-262.10	-23.53
18	-30.0	15.78	44.38	-428.55	-12.17	-113.75	-26.24
19	-16.5	18.94	169.40	-283.37	37.84	-51.77	-11.21
20	-29.4	108.50	81.08	800.68	2.69	58.83	13.47
21	-33.6	23.66	150.64	331.61	55.35	29.86	52.98

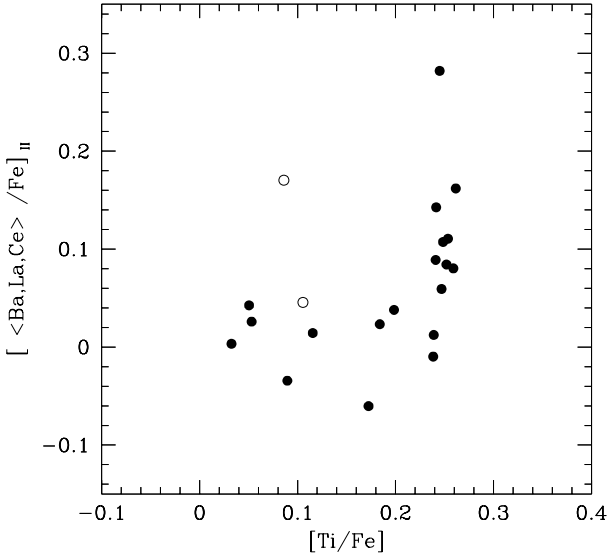


Fig. 9. Correlation diagram for $[< Ba, La, Ce > / Fe]_{II}$ versus $[Ti/Fe]$

As we have seen earlier, the two stars HD 193901 and HD 194598 represented by open symbols in the correlation diagrams, display a number of abundance anomalies: a lower Ni abundance (Fig. 5b), a probable overabundance in heavy *s*-process elements (Fig. 9) and, above all,

a higher abundance in *r*-process products (Figs. 7b, 10). If, as stated by Anders and Grevesse (1989), Ni is the even iron peak element with the smallest contribution from explosive nucleosynthesis, this behaviour might be explained by a different nucleosynthetic history, namely an enhanced contribution from explosive processes compared to equilibrium ones.

8. Kinematics of the stars

The kinematical data are summarized in Table 9. The radial velocities were selected from several sources: Barbier-Brossat et al. (1994), Wilson (1953), Evans (1967), Gratton and Sneden (1991), Lindgren and Andersen (private communications). The radial velocities are known to about $\pm 2 \text{ km s}^{-1}$ for most of the stars. The proper motions and parallaxes used to calculate the galactic velocities were taken from the Hipparcos Catalogue (1997). The calculation of the galactic space velocities U, V and W with respect to the LSR is based on the method presented in Johnson and Soderblom (1987). The corrections applied to the observed velocities for the solar motion are $(-10.4, +14.8, +7.3) \text{ km s}^{-1}$ in (U,V,W) (Mihalas and Routly 1968).

Upon examination of Table 9, our sample appears to contain thick disk and halo stars. However, there is no clear distinction between these two populations in Figs. 7a, 8 and 9, since thick disk stars are found on both branches in these plots.

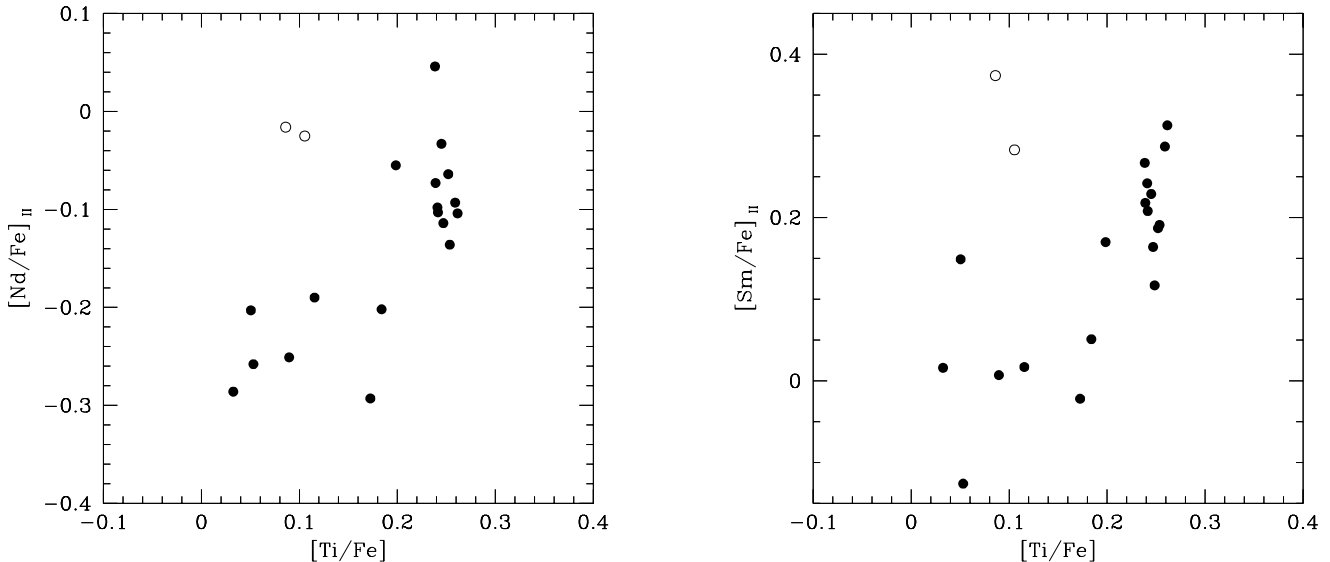


Fig. 10. Correlation diagrams for $[\text{Nd}/\text{Fe}]_{\text{II}}$ and $[\text{Sm}/\text{Fe}]_{\text{II}}$ versus $[\text{Ti}/\text{Fe}]$

This result seems to disagree with the analysis of Nissen and Schuster (1997, NS), who have selected two samples of stars on the basis of their kinematical properties and covering about the same metallicity range as ours. While their halo stars are indeed found in both branches of our diagram, all their disk stars display maximum $[\alpha/\text{Fe}]$ values. Some of our disk stars undoubtedly have low $[\alpha/\text{Fe}]$. The apparent disagreement might be due to the fact that both samples contain a relatively small number of stars and that, by accident, all disk stars selected by NS have a high $[\alpha/\text{Fe}]$.

It may be of interest to note that the two stars which seem to display some anomalous abundances are just these which have the most halo-like kinematic properties. However, it is difficult to conclude on the basis of only two stars. We plan to extend the analysis to other metal-poor stars with kinematics more typical of the halo.

9. The “Two branches diagram”

9.1. Universality of the “Two branches diagram”

The analysis of the correlations between the relative abundances of a number of elements for stars with roughly 0.1 of the solar metallicity leads us to distinguish between two stellar populations, corresponding to distinct branches in the diagram (e.g. Fig. 7a): (a) a fraction of the stars have a range of moderate overabundances of the α -elements and either a constant or slowly varying abundance of the s -process elements relative to the iron peak, and (b) the others show a constant (and maximum) overabundance of the α -elements relative to the iron-peak elements, and a range in s -process abundances. This behaviour must be related to nucleosynthesis processes.

Since our sample contains a limited number of stars, its astrophysical significance may be checked by including the results of other analyses. In Fig. 11, we have added the NS stars as well as the sample of Zhao and Magain (1991, ZM). The quality of those data is almost as good as the quality of the data presented here. The ZM data extend our sample towards stars of lower metallicity. The stars in Fig. 11 have metallicities $-2 \leq [\text{Fe}/\text{H}] \leq -0.6$. The zero points have been fixed by comparing the results obtained for the stars in common (3 with NS, 10 with ZM), for which we have kept the results obtained here with a more precise analysis. We see that all these metal-poor stars follow the same trend, independently of their metallicity.

As our metallicity range for (thick) disk stars is rather limited towards metal-poor stars, we have added in Fig. 12 the data obtained by Edvardsson et al. (1993) for disk stars of various metallicities. The difference in zero-points between the two analyses has been corrected on the basis of 10 stars in common. We see that these disk stars definitely *do not* follow the relation obtained for metal-poor stars, but scatter mostly through the upper left part of the diagram. Taking into account the larger error bars in Edvardsson et al. (1993) data, our metal-poor stars define the lower right envelope of this domain. This envelope also contains the lowest metallicity stars of Edvardsson et al. (1993).

On the basis of these two comparisons, a cutoff in metallicity at $[\text{Fe}/\text{H}] \sim -0.6$ seems to emerge. For stars of higher metallicity, the *two branches diagram* does not apply. Lower metallicity stars follow a universal relation described by the *two branches diagram*. We shall refer to the slowly varying branch stars as Population IIa and to the vertical branch as Population IIb.

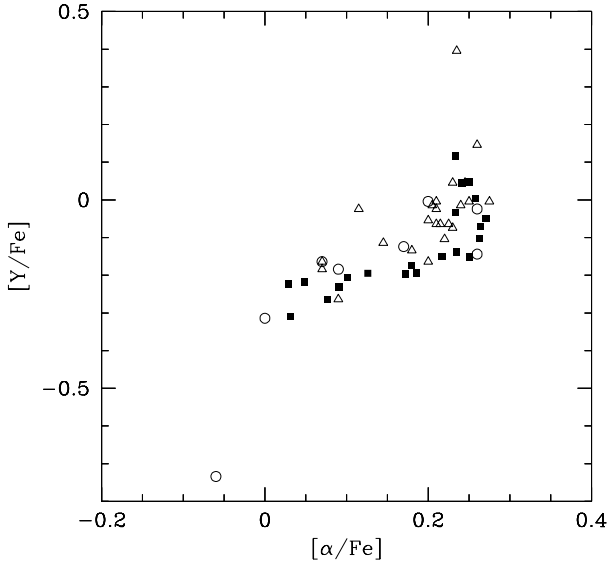


Fig. 11. Correlation diagram for $[Y/Fe]$ versus $[\alpha/Fe]$ with our data (full squares), the data of Zhao and Magain (1991) (open circles) and the data of Nissen and Schuster (1997) (open triangles). Only stars with $[Fe/H] < -0.6$ are plotted

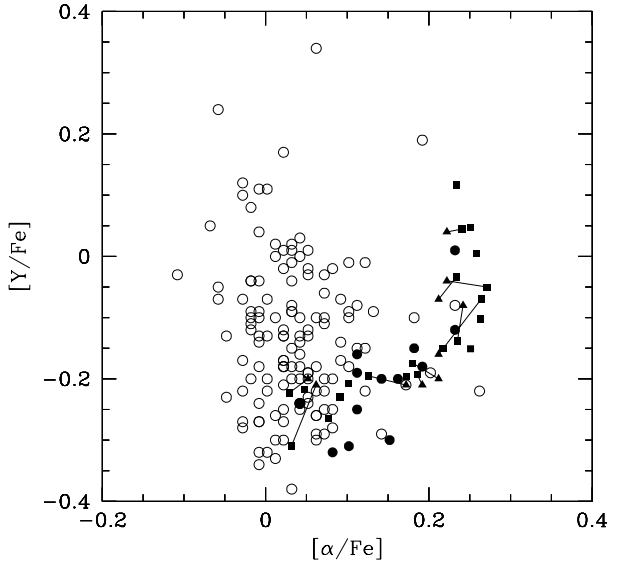


Fig. 12. Correlation diagram for $[Y/Fe]$ versus $[\alpha/Fe]$ with our data (full squares), the data of Edvardsson et al. (1993) for $[Fe/H] > -0.6$ (open circles), for $[Fe/H] < -0.6$ (full circles) and for the stars also included in our work (full triangles), joined by lines to their counterparts

9.2. Interpretation

9.2.1. General picture

We now briefly describe a possible scenario for the formation and origin of these metal-poor stars, which provides an explanation for the universal relation described above. This scenario will be developed in more details in a forthcoming paper. It takes place in the early stages of the chemical evolution of the Galaxy. We distinguish two separate phases in the evolution of the metal-poor stars.

Phase 1

At first, we assume that there is a burst of star formation, consisting essentially of massive stars. As these stars evolve and become supernovae (SNe), α -elements and r -process elements are formed and then ejected in the surrounding interstellar matter (ISM). New stars are formed from this ISM, which is enriched in those α and r -process elements. These stars correspond to Pop IIa.

Phase 2

As time goes on, the lower mass stars are either still contracting towards the main sequence or have reached a more evolved phase, maybe already processing s elements. These evolved stars are known to have strong stellar winds and to undergo superwind events. The newly formed s elements are thus ejected into the surrounding ISM, previously enriched in α - and r -process elements. New born stars formed from this ISM will keep a constant value for

$[\alpha/Fe]$ but will be enriched in s elements. They will belong to Pop IIb.

Another possibility is that already formed lower mass stars can accrete gas from the s -process enriched winds. In this case, the s -process enrichment will show up in the external layers only, at least if the convective envelope is not too large. These stars will also belong to Pop IIb, although their internal chemical composition will be that of Pop IIa at the bottom of the vertical branch.

9.2.2. Globular cluster scenario

In this subsection, we will be more specific as to the environment in which our two-phases scenario could occur.

As we have shown in Section 9.1, the *two branches diagram* seems to define a universal relation for stars more metal-poor than $[Fe/H] \sim -0.6$. In particular, it should therefore apply to all halo stars.

Since the halo is also populated by globular clusters (GCs, see the recent review by Meylan & Heggie 1997), we have searched for a connection between them and the field halo stars (FHS), and we propose the following EASE (Evaporation/Accretion/Self-Enrichment) scenario:

- (1) all FHS were born in (proto-) GCs;
- (2) GCs have undergone a chemical evolution;
- (3) some of the GCs were disrupted at an early stage in their evolution, the lower mass stars forming Pop IIa;
- (4) in the GCs which have survived, accretion of matter from AGB stars modifies the surface composition of the

cluster stars;

(5) some low mass stars evaporate from the GCs or get dispersed in the halo when the GC is disrupted. They form Pop IIb FHS.

The relation between the thick disk and field halo stars on the one hand and GCs on the other hand is substantiated by the similarities in kinematic properties and metallicity distributions between:

- (1) the FHS and the GCs more metal-poor than $[\text{Fe}/\text{H}] \sim -1$ (“halo GCs”);
 - (2) the thick disk stars and the GCs more metal-rich than $[\text{Fe}/\text{H}] \sim -1$ (“disk GCs”);
- (Zinn 1985, Armandroff 1989, Harris 1998).

A few authors (Cayrel 1986; Smith 1986, 1987; Morgan and Lake 1989) have considered the possibility of GCs self-enrichment by SNe and, through simple and qualitative arguments, have shown that this was indeed possible under certain conditions.

In a recent paper, Brown et al. (1995) have developed a more detailed model for the early dynamical evolution and self-enrichment of GCs which supports the first part of our scenario. They show that the SN explosions of the first generation stars trigger the formation of an expanding shell, decelerated by the surrounding hot ISM, in which second generation stars can form. They also discuss the conditions for a GC to survive this phase of chemical self-enrichment.

While the second generation stars are forming, the proto-GC may become unstable and disruption can occur. This can happen at any time during the SNe phase. It is important to notice that, at the time of disruption, the metallicity is fixed by the rate of mixing of the enriched matter expelled by SNe with the pre-existing ISM, i.e., by the ratio of the mass of the processed material to the mass of the ISM. On the other hand, the value of $[\alpha/\text{Fe}]$ depends on the mass distribution of the Type II SNe which have exploded by the time of disruption. Of course, only the less massive stars are still visible now. They form Pop IIa and they appear somewhere on the slowly varying branch, depending on the time at which disruption of the proto-GC occurred. All stars originating from a given proto-GC should have the same $[\alpha/\text{Fe}]$ value but stars coming from different proto-GCs will have different values. Since the disrupted proto-GC has not completed its chemical evolution, some of the stars dispersed in the halo may have a much lower metallicity than the lowest ones presently observed in the GCs, independently of their respective $[\alpha/\text{Fe}]$.

The GC can also survive the SNe phase. When all stars more massive than about $8 M_{\odot}$ have exploded as SNe, the α and r elements synthesis stops, leading to a typical value of $[\alpha/\text{Fe}]$. Such a view is supported by the analysis of Carney (1996) who finds that GCs do not show any significant variations in $[\alpha/\text{Fe}]$ despite wide variations in $[\text{Fe}/\text{H}]$, age and kinematics.

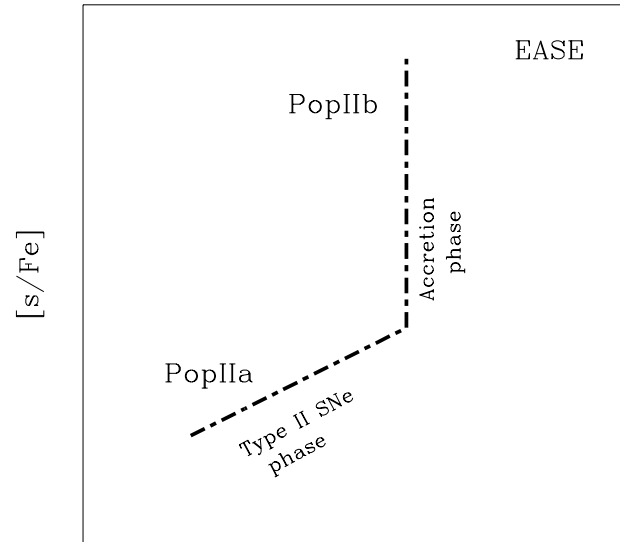


Fig. 13. EASE scenario. $[\alpha, r/\text{Fe}]$

According to Fig. 7, our scenario requires this typical value of $[\alpha/\text{Fe}]$ to be the maximum value observed in the *two branches diagram*, which in turn implies an increase of $[\alpha/\text{Fe}]$ with time in a given proto-GC. The end of the SNe phase must indeed correspond to the bottom of the vertical branch. Such an increase with time, i.e., with decreasing mass of the progenitor, is in agreement with the theoretical yields computed by Woosley & Weaver (1995) although such results are still rather uncertain since other computations (e.g. Thielemann et al. 1993) show different behaviours. Moreover, such an interpretation of Fig. 7 implies a nearly solar $[\text{Ti}/\text{Fe}]$ for the most massive SNe, which is also in agreement with some of the models computed by Woosley & Weaver (1995).

The fact that $[\text{Y}/\text{Fe}]$ increases with $[\text{Ti}/\text{Fe}]$ for Pop IIa stars would indicate that the ratio of the Y yield to the Fe yield increases with decreasing mass of the SN progenitor (Fig. 7). On the other hand, the roughly constant value obtained for the heavy s elements (Ba, La, Ce) observed in Fig. 9 suggests that the ratio of the yields (Ba, La, Ce)/Fe does not vary significantly with the mass of the progenitor.

In a second phase, intermediate mass stars evolve until they reach the AGB where they enrich their envelope in s-process elements due to dredge-ups during the thermal pulses. Through stellar winds or superwinds, those enriched envelopes are ejected and they pollute the surrounding less massive stars by accretion.

No new stars would be formed at this stage because the remaining ISM is probably too diffuse. During the subsequent evolution of the GC, some of these surface enriched low mass stars evaporate and form Pop IIb. Those stars can also get dispersed in the halo when the GC gets disrupted (e.g., when crossing the disk).

For a typical r element like Eu, the behaviour of $[\text{Eu}/\text{Fe}]$ versus $[\alpha/\text{Fe}]$ (Fig. 7) is completely different, showing a perfect correlation in Pop IIa stars and an absence of the vertical s -process feature, replaced by a clumping of the points representative of Pop IIb stars at the constant value of $[\alpha/\text{Fe}]$ and $[r/\text{Fe}]$, characteristic of the end of the massive stars outburst. This shows that, if also produced by lower mass stars, it must be in roughly the same proportions as Fe.

Our EASE scenario nicely explains the features observed in the *two branches diagrams*. It is schematically displayed in Fig. 13.

Pop IIa stars mostly originate from disrupted proto-GCs, their $[\alpha/\text{Fe}]$ depending on the moment at which disruption occurs. Pop IIb stars escape later in the evolution of the cluster, after the end of the SN phase.

This EASE scenario can also explain the larger metallicity range covered by the FHS, extending to much lower metallicities than the GCs. The very metal-poor stars have escaped from the proto-GCs at a very early stage of the outburst phase, when the chemical enrichment of the cloud was still very low.

Acknowledgements

This work has been supported by contracts ARC 94/99-178 “Action de Recherche Concertée de la Communauté Française de Belgique” and Pôle d’Attraction Interuniversitaire P4/05 (SSTC, Belgium). We wish to thank J. Andersen and H. Lindgren for providing radial velocities for some of the stars and N. Grevesse and J. Sauval for some of the atomic data. We also thank N. Grevesse and G. Meylan for fruitful discussions. The Simbad database, operated at CDS, Strasbourg, France, has been used in this project.

References

- Alonso, A., Arribas, S., Martinez-Roger, C. 1994, *A&ASS*, 107, 365
- Anders, E., Grevesse, N. 1989, *Geochimica et Cosmochimica Acta*, 53, 197
- Andersen, T., Poulsen, O., Ramanujam, P.S., Petrakiev-Petkov, A. 1975, *Sol. Phys.*, 44, 257
- Armandroff, T.E. 1989, *AJ*, 97, 375
- Arnesen, A., Bengtsson, A., Halling, R., Lindskog, J., Nordling, C., Noreland, T. 1977a, *Phys. Scr.* 16, 31
- Arnesen, A., Bengtsson, A., Halling, R., Noreland, T. 1977b, *J. Phys. B*, 10, 565
- Arnett, D. 1991, in *Frontiers of Stellar Evolution*, ASP Conf. Ser. 20, 389
- Barbier-Brossat, M., Petit, M., Figon, P. 1994, *A&ASS* 108, 603
- Becker, O., Enders, K., Werth, G., Dembczynski, J. 1993, *Phys. Rev. A*, 48, 3546
- Biémont, E., Grevesse, N., Lowe, R.M., Hannaford, P. 1981, *ApJ* 248, 867
- Biémont, E., Kerner, C., Meyer, G., Träger F., zu Putlitz G. 1982, *A&A* 107, 166
- Biémont, E., Grevesse, N., Hannaford, P., Lowe, R.M. 1989, *A&A* 222, 307
- Blackwell, D.E., Shallis, M.J. 1977, *MNRAS* 180, 177
- Blackwell, D.E., Menon, S.L.R., Petford, A.D. 1984, *MNRAS* 207, 533
- Blackwell, D.E., Petford, A.D., Simmons, G.J. 1982a, *MNRAS* 201, 595
- Blackwell, D.E., Booth, A.J., Menon, S.L.R., Petford, A.D. 1986a, *MNRAS* 220, 289
- Blackwell, D.E., Booth, A.J., Menon, S.L.R., Petford, A.D. 1986b, *MNRAS* 220, 303
- Blackwell, D.E., Booth, A.J., Petford, A.D., Shallis, M.J., Leggett, S. 1982b, *MNRAS* 199, 21
- Broström, L., Mannervik, S., Royen, P., Wännström A. 1995, *Phys. Scr.* 51, 330
- Brown, J.H., Burkert, A., Truran, J.W. 1995, *ApJ*, 440, 666
- Carney, B.W. 1983, *AJ* 88, 623
- Carney, B.W. 1996, *PASP* 108, 900
- Cayrel, R. 1986, *A&A* 168, 81
- Corliss, C.H., Bozman, W.R. 1962, *Experimental Transition Probabilities for Spectral lines of Seventy Elements* (NBS Monograph 32) (Washington: GPO)
- Doerr, A., Kock, M. 1985, *J. Quant. Spectrosc. Radiat. Transfer*, 33, 307
- ESA, 1997, ‘The HIPPARCOS Catalogue’, ESA SP-1200, ESTEC, Noordwijk
- Edvardsson, B., Andersen, J., Gustafsson, B., Lambert, D.L., Nissen, P.E., Tomkin, J. 1993, *A&A*, 275, 101
- Evans, D.S. 1967, *Catalogue of Stellar Radial Velocities*, IAU Symp. 30, 57
- Gallagher, A. 1967, *Phys. Rev.* 157, 24
- Gosset, E., Magain, P. 1993, *ESO Messenger* 73, 13
- Gratton, R.G., Sneden, C. 1991, *A&A* 241, 501
- Gratton, R.G., Sneden, C. 1994, *A&A* 287, 927
- Gray, D.F. 1972, *The Observation and Analysis of Stellar Photospheres*, Wiley, New York
- Grevesse, N., Noels, A., Sauval, A.J. 1996, *Cosmic Abundances*, ASP Conf. Series, Vol. 99, 117
- Gustafsson, B., Bell, R.A., Eriksson, K., Nordlund, A. 1975, *A&A* 42, 407
- Hannaford, P., Lowe, R.M., Grevesse, N., Biémont, E., Whaling, W. 1982, *ApJ* 261, 736
- Harris, W.O. 1998, preprint astro-ph/9801201
- Jehin, E., Magain, P., Neuforge, C., Noels, A., Thoul, A.A. 1998, *A&A* 330, L33
- Johnson, D.R.H., Soderblom, D.R. 1987, *AJ*, 93, 864
- Kurucz, R.L. 1993, *ATLAS9 Stellar Atmosphere Programs and 2 km/s grids*, Kurucz CD-ROM No 13
- Magain, P. 1987, *A&A* 181, 323
- Meylan, G., Heggie, D.C. 1997, *Astron. Astrophys. Rev.*, 8, 1
- Migdalek, J., Baylis, W.E. 1987, *Can. J. Phys.* 65, 1612
- Mihalas, D., Routly, P.M. 1968, *Galactic Astronomy*, Freeman and Co.
- Möller, W., Hürnermann, H., Alkhazov, G., Panteleev, V. 1993, *Phys. Rev. Lett.* 70, 541
- Morgan, S., Lake, G. 1989, *ApJ*, 339, 171
- Nissen, P.E., Schuster, W.J. 1997, *A&A*, 326, 751
- Nissen, P.E., Høg, E., Schuster, W.J. 1998, *Proc. of Hipparcos Venice 97 Symposium*, ESA SP-402, in press

- Olsen, E.H., 1994, A&AS 106, 257
- Schuster, W.J., Nissen, P.E. 1988, A&ASS 73, 225
- Smith, G. 1986, PASP, 99, 67
- Smith, G. 1987, ApJ, 306, 565
- Smith, G., Raggett, D. St J. 1981, J.Phys. B: At. Mol. Phys. 14, 4015
- Thielemann, F.K., Nomoto, K., Hashimoto, M. 1993, in *Origin and Evolution of the Elements*, eds. N. Prantzos et al., Cambridge Univ. Press, p.297
- VandenBerg, D.A., Bell, R.A. 1985, ApJSS 58, 561
- Villemoes, P., Wang, M. 1994, Z. Phys. D, 30, 19
- Whaling, W., Hannaford, P., Lowe, R.M., Biémont, E., Grevesse, N. 1985, A&A 153, 109
- Wickliffe, M.E., Lawler, J.E. 1997, ApJSS 110, 163
- Wilson, R.E. 1953, General Catalog of Stellar Radial Velocities, Carnegie Inst. of Washington, Washington, D.C.
- Wiese, W.L., Martin, G.A. 1980, NSRDS-NBS 68 (U.S. Gov. Printing Office, Washington, DC)
- Woolf, V.M., Tomkin, J., Lambert, D.L. 1995, ApJ 453, 660
- Woosley, S.E., Weaver, T.A. 1995, ApJSS 101, 181
- Zhao, G., Magain, P. 1991, A&A 244,425
- Zinn, R. 1985, ApJ, 293, 424